Turbulent flow interaction with a circular cylinder

Reza Maryami*
Yazd University, Yazd, Iran
Syamir Alihan Showkat Ali†
School of Manufacturing Engineering, University Malaysia Perlis, Malaysia
Mahdi Azarpeyvand‡
Faculty of Engineering, University of Bristol, BS8 1TR, UK
Abbas Afshari§
Yazd University, Yazd, Iran
Ali A. Dehghan¶
Yazd University, Yazd, Iran

A comprehensive experimental study is carried out to investigate the unsteady pressure exerted on the surface of a round cylinder in the sub-critical Reynolds number range. Experiments are performed using a highly instrumented cylinder, with several static pressure taps and dynamic pressure transducers at different spanwise and peripheral locations, enabling extensive dynamic surface pressure, coherence and turbulence length-scale analysis. The effects of the free-stream turbulence are investigated by placing the smooth and turbulent-generating grids within the contraction region of the wind tunnel. For both incident flows, the surface pressure results show the emergence of the fundamental, first and second harmonics at most peripheral angles, while at the cylinder base the surface pressure spectra is dominated by the first harmonic. The amplitudes of the fundamental and second harmonic tones are observed to peak within the turbulent boundary layer region and then decrease toward the base, while that of the first harmonic is observed increases with the angle and peaks at the cylinder base. The spanwise coherence results have also shown that the vortex shedding structures have a long spanwise length, while the three-dimensional flow structures within the boundary layer have a much shorter correlation length. Furthermore, the spanwise coherence at the cylinder base is found to be purely tonal. The use of the turbulence grids is shown to lead to slight shift in the vortex shedding frequencies to lower frequencies. It has also been observed that the flow structures in turbulent incident flow have higher energy level compared to the smooth incident flow.

Nomenclature

B	wind tunnel blockage ratio
C_p	Surface pressure coefficient
C_{p_b}	base pressure coefficient
D	cylinder diameter $[m]$
d	grid rod diameter $[m]$
f	frequency [Hz]
f_0	fundamental vortex shedding frequency [Hz]
f_1	first vortex shedding harmonic [Hz]

*Ph.D Student, School of Mechanical Engineering, r.maryami@gmail.com
†Senior Lecturer, Manufacturing Engineering, syamir@unimap.edu.my
‡Reader in Aeroacoustics, Mechanical Engineering, m.azarpeyvand@bristol.ac.uk
§Ph.D Student, School of Mechanical Engineering
¶Associate Professor, School of Mechanical Engineering

f_2	second vortex shedding harmonic [Hz]
f_s	sampling frequency [Hz]
L_c	equivalent coherence length [m]
N_r	number of sample records
p	pressure fluctuations [Pa]
p_∞	free stream smooth flow pressure [Pa]
$p_\infty^{'}$	free stream turbulence flow pressure [Pa]
R_{pp}	surface pressure autocorrelation
R_{uu}	velocity autocorrelation
Re	Reynolds number
St	Strouhal number $[fD/U_\infty]$
U_∞	free stream velocity $[m/s]$
t	time $[s]$
x, y, z	streamwise, normal and lateral coordinate $[m]$
$\gamma^2_{pi,pj}$	coherence function
η_z	spanwise microphone separation distance $[m]$
θ	peripheral angle [deg]
θ_m	angular position of minimum pressure [deg]
θ_s	separation angle [deg]
Φ_{pp}	surface pressure power spectral density $[Pa^2/\text{Hz}]$
$\Phi_{pi,pj}$	surface pressure cross-spectrum $[Pa^2/\text{Hz}]$
$\Phi_{pi,pi}$	surface pressure auto-spectrum $[Pa^2/\text{Hz}]$
Λ_{pp}	spanwise length scale $[m]$
Λ_{uu}	turbulence length scale $[m]$
σ	Grid solidity
ν	kinematic viscosity $[m^2/s]$
τ	time delay $[s]$
PSD	Power Spectral Density

I. Introduction

The aerodynamics of circular cylinders placed in a laminar cross-flow has extensively been studied[1] as it involves some very interesting physics and is of great importance in many engineering applications, including risers in marine engineering, buildings, bridges, tubular heat exchangers, power transmission lines, chimneys, towers and so on. The noise generation mechanism and methods to reduce noise from bluff bodies is also of great academic and industrial interest.[2–11] While the aerodynamics of bluff bodies has been the subject of much experimental studies, there still exists a need for high-quality measurement of the quantities important for the understanding of the noise generation mechanism.

The Aeolian tones, the tonal noise generated due to the vortex shedding, are known is a basic and important characteristic of the aerodynamic of bluff bodies. The effects of free-stream turbulence flow on the vortex shedding from the cylinder have been investigated in the literature but many features are still unclarified. Bearman and Morel[12] reviewed some influences of turbulent incident flow on dynamic flow around bluff bodies at high Reynolds number. It is well recognized that sub-critical regime (*i.e.* $Re = 300 - 2 \times 10^5$) is described by purely laminar separation and turbulent vortices formation in downstream. Bloor[13] drew firstly attention to this transition and reported that it moves upstream with increase in turbulence intensity and/or Reynolds number. The transition leads to increase mixing and implies that vortex formation takes place closer to the cylinder base.[14] The decrease in base pressure and increase in the fluctuating forces also associated with shrinking of the formation region. The experimental study performed by Norberg and Sunden[15] provided useful results concerning the effects of Reynolds number and turbulence intensity on the fluid forces acting on a circular cylinder in cross flow. For $Re < 10^5$, increase in pressure forces observed with increasing turbulence intensity and opposite trend occurred for higher Reynolds number. In order to establish accurate data on the fluctuating pressure distributions root-mean-square (rms) forces in sub-critical flow, experiments carried out by West and Apelt[5] on smooth circular cylinder. The result showed that the effects of changes of free-stream turbulence on rms pressure distributions, rms lift coefficient and mean drag coefficient is similar to the influences of increase in Reynolds number. Moreover, suggested that as well as

turbulence intensity, the scale and spectrum of the turbulence are noticeable parameters.

The most conventional and effective method for measuring the unsteady surface pressure fluctuations acting on the surface in a flow field is the use of miniature pressure transducers. A comprehensive study of vortex shedding noise from a single cylinder using this method was carried out by Schlinker et al.[3] Results had confirmed that vortex shedding is dependent on the surface roughness and the effective Reynolds number. The wall pressure fluctuation measurements using in-situ pressure transducers were also reported in the work by Casalino and Jacob[16] for understanding of the statistical characteristics of the wake flow structures. In this research argued that both the fundamental vortex shedding frequency and the second harmonic correspond to the lift fluctuations of the cylinder, while the first harmonic is related to the drag fluctuation force acting on the cylinder. Using the same measurement technique, Oguma et al.,[10] Fujita et al.[17] and Ackerman et al.[18] carried out an investigation on the properties of the Aeolian tone and the surface pressure fluctuations for a wide range of Reynolds numbers.

Stowell and Deming[7] were the first to measure the directivity of the noise radiated by circular cylinders and demonstrated that the sound field has a dipolar character, with peaks normal to the free-stream flow direction and the cylinder axis. The mathematical model developed by Curle[19] showed that the fluctuating forces acting on the cylinder, as a result of the solid-flow interaction, leads to a dipolar radiation. Curle's dimensional analysis also showed that theoretically the sound intensity scales with the sixth-power of the velocity. Based on Curle's mathematical model for the prediction of noise from stationary solid bodies in a flow, one can infer that the far-field sound from a circular cylinder is directly related to the surface integral of the unsteady pressure exerted on the body of the cylinder as a result of the interaction with the boundary layer and wake structures.[10] Therefore, for proper understanding of the noise generation mechanism from external bodies in a flow, it is important to study the flow-field around the object and the unsteady forces exerted by flow structures.

As reviewed above, most of the work done to data has been experimental, with the majority of it in wind tunnels in flows with low levels of free-stream turbulence. Unfortunately, there is no a comprehensive study to investigate the surface pressure fluctuations over the circumference of the cylinder and along its span in turbulent incident flow. This paper aims to provide an extensive body research of the unsteady pressure exerted on the surface of circular cylinders in a turbulent cross-flow in the subcritical flow regime and perform comprehensive near-field correlation studies to improve our understanding of the noise generation mechanisms from bluff bodies. The experimental setup and wind tunnel tests are described in Sec. II. The results and discussions are detailed in Sec. III.

II. Measurement Setup

The flow experiments were performed in an open-jet subsonic wind tunnel facility of the Yazd University. The wind tunnel has an exit cross-sectional area of $0.46\ m \times 0.46\ m$ with a maximum reliable wind speed of $25\ m/s$ and a turbulence level of less than 0.3%. The internal walls of the wind tunnel were equipped with a highly absorbing porous layer[20] to avoid noise contamination due to the fan background noise. The reduction of the fan background noise was found to be about 15 dB over a wind range of frequencies of interest.

A. Cylinder configuration

The flow measurements have been carried out using a circular cylinder with an outer diameter of $0.022\ m$ and a span length of $0.46\ m$. The circular cylinder test-rig is made of three different parts consisting of one middle section with static and dynamic surface pressure instrumentations and two side extension parts, *i.e.* extend to that of the span length of the wind tunnel exit cross-sectional area. The layout of the circular cylinder test-rig is shown in Fig. 1. In order to eliminate the wind tunnel walls effects on the measured quantities, the model was built with an aspect ratio (span length to diameter) of over 20.[21] The blockage ratio of the cylinder was found to be less than 5%. The cylinder was properly placed within the potential core of the jet flow and was held by two parallel rectangular side-plates to avoid the possibility of vibration. In order to collect the flow and pressure data in fine angular increments, *i.e.* at every 5^o degrees, the test-rig was mounted on a turning table.

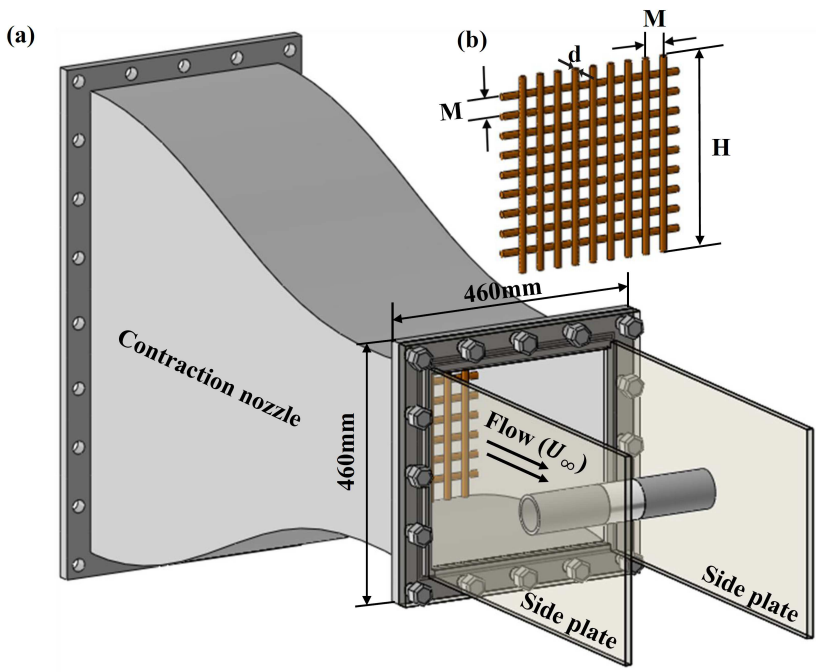

Figure 1: (a) The geometry of the contraction nozzle and the experimental setup, (b) turbulence-generating grid.

B. Surface pressure instrumentation

The cylinder was instrumented with several Panasonic electret condenser pressure transducer (series WM-61A) for the measurement of the unsteady surface pressure fluctuations. The transducers have a diameter of 0.006 m, height of 0.0034 m and circular sensing area of 0.002 m. The pressure transducers used in the present work are similar to that of the transducers used in,[22] which has shown to produce reliable pressure data in the frequency range of interest. In order to reduce and eliminate the pressure attenuation effects at high frequencies, the pressure measurements were carried out using a small pinhole with very small diameter at the surface of the cylinder.[2,9,23] The pressure transducers are placed underneath a small pinhole mask of 0.00055 m diameter and fixed inside the cylinder using a fully sealed holding mechanism, see Fig. 2. A total number of 15 pressure transducers are distributed in the peripheral and spanwise directions of the cylinder. The layout of the pressure transducers are shown in Fig. 2. In order to verify the two-dimensionality of the flow and to measure the spanwise length scale of the flow structure, a set of transducers (*p1-p8*) are installed along the span of the cylinder. The transducers in the spanwise direction are placed with an unequal spacing, which provides a non-redundant population of sensor spacing and maximum number of spatial distances used for correlation studies.[4] The spanwise transducers are distributed over 5 D - 7 D to enable the flow structures to be fully resolved.[17,22,24] It is important to ensure that the transducers are kept outside of the boundary layer developed by the side-plates. In this study, the maximum boundary layer thickness formed via the effect of the side-plates at the flow velocity of $U_\infty = 20\ m/s$ was found to be 0.008 m. In order to better understand the flow structures and flow shedding at different peripheral angles, several pressure transducers (*p9-p15*) are distributed around the circumference of the cylinder at the mid-span plane with an angular spacing of 45^o. The locations of the pinhole transducers are summarized in Table 1. The transducers were calibrated in-situ based on the method described in Ref.,[2,25] and the calibration was performed before and after each measurement. A 16-channel NI PCI-6023E data acquisition system was used to collect the surface pressure fluctuations data, with a sampling frequency of 40 kHz and measurement time of 60 seconds. In order to reduce the statistical convergence error, the pressure spectra were calculated based on the average spectra of individual data obtained from dividing the time series pressure data into a sequence of records,[26] *i.e.* $1/\sqrt{N_r}$, N_r is the number of records. In the present work, a total number of N_r=800 records were used, with an uncertainty of about 3.5%.

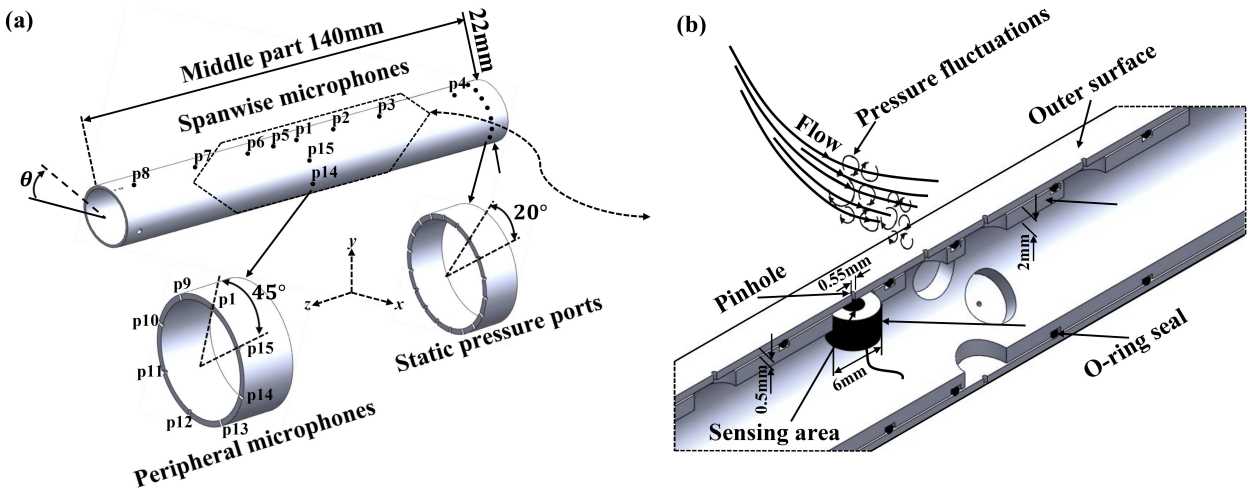

Figure 2: (a)In-situ boundary layer surface pressure measurement using a pressure transducer installed under a pinhole and (b) The sensing area on the cylinder equipped with static pressure taps and spanwise and peripheral pressure transducers.

Table 1: Position of pressure pinholes on the surface of model.

Transducers	z/D	θ **(deg.)**	**Transducers**	z/D	θ **(deg.)**
p1	0.0	90	*p9*	0.282	45
p2	0.682	90	*p10*	0.0	0
p3	1.545	90	*p11*	0.282	-45
p4	2.955	90	*p12*	0.0	-90
p5	-0.41	90	*p13*	0.282	-135
p6	-0.91	90	*p14*	0.0	180
p7	-1.864	90	*p15*	0.282	135
p8	-3.0	90	-	-	-

C. Static pressure measurement

In order to better understand the flow field and the pressure distribution (C_p) around the cylinder, the test-rig was instrumented with 18 static pressure taps, which are distributed evenly with an angular spacing of 20^o over the circumference of the cylinder, see Fig. 2. The static pressure taps have a diameter of 0.00055 m. Each of the pressure tap was tightly fitted with a 0.005 m brass tube, with the inner and outer diameters of 0.0004 m and 0.0006 m, respectively. The brass tubes are connected to polyurethane tubes, and finally connected to the pressure scanner ports. A 16 channels Honeywell electronic differential pressure measurement unit with the system accuracy of $\pm$ 1.25 kPa was used to perform the static pressure measurements. An uncertainty analysis was carried out, based on the method described in Ref.,[27] and the uncertainty was found to be below 2.2%.

D. Characterization of grid turbulence

In the present work, three biplane grids with different mesh sizes were used to generate the incoming turbulence flow, upstream of the circular cylinder model. The shape of the grid elements can have important effects on the homogeneity, intensity level and the stability of the wake system generated by the grid elements.[28] It was shown that the biplane grids are able to generate turbulence with the ratio between the streamwise and lateral turbulence intensities ($\overline{u'^2}/\overline{v'^2}$) is much closer to unity,[29] which is not found for the

grids with other different shape or geometries. In order to ensure the production of approximately homogeneous region, Corrsin[28] suggested that the grid must be designed such that $H >> M$, where H is the wind tunnel cross-section dimension and M is the mesh length of the grid. According to this criteria, the mesh size for the biplane grids constructed in this study are of 0.04 m, 0.056 m and 0.09 m each. The diameter of the round rods are determined based on the mesh size ratio, $M/d \approx 5$.[30] The rods with the diameters of 0.009 m, 0.0127 m and 0.0203 m were chosen for the turbulence grids in this study. The grid solidity ratio (σ) is another important criteria that should be considered in manufacturing the biplane grids. Laws and Livesey[30] stated that the grids with a grid solidity ratio of about σ=0.3-0.4 are typically used to generate turbulence that is homogeneous and isotropic at sufficiently large distances downstream from the grid. The specific grid sizes, rod diameters, and the solidity ratios are summarized in Table 2.

Table 2: Physical properties of turbulence grid generator.

Grids	d (m)	M (m)	M/d	σ
Grid 1 (G9)	0.009	0.040	5	36
Grid 2 (G12)	0.0127	0.0564	4.43	40
Grid 3 (G20)	0.0203	0.090	4.43	40

Basically, three different flow field regions can be categorized downstream of the turbulence grid. The first region corresponds to the flow developing region nearest the grid where the wakes from the rod merges. The flow in this region is inhomogeneous and anisotropic, and consequently, the production of turbulent kinetic energy is observed.[31] The second region is dominated by flow which is nearly homogeneous, isotropic and nearly isotropic and is in this region that the energy is transferred from one wavenumber to another. Depending on the Reynolds number of the flow, the second region was found to be reached at a distance, x, downstream of the grid ranging from 10 M-50 M.[32,33] This region was found to be the appropriate location for the positioning of the circular cylinder, downstream of the grid in the present work. The third region corresponds to the decay region, where the viscous effects dominate the large energy containing turbulence length scales in the furthest downstream locations from the grid. Corrsin[28] suggested that for grids with a relatively low solidity, the flow measurements should be performed at $x/M \geq 40$. However, several empirical studies have shown that the second region may exist as early as $x/M \approx 20$.[34–36] In the present study, the flow measurement locations of all the three biplane grids were chosen along the center line of the tunnel for $20 \leq x/M \leq 80$ according to the methods obtained in.[37]

In order to study the effect of turbulence length scale on the surface pressure fluctuations, the circular cylinder was located at the positions of $x/D = 7.27$ and $x/D = 12.27$, downstream of the biplane Grids 1 and 2, respectively. These two locations correspond to the turbulence length scale of $\Lambda_{uu} \approx 0.5D$ and $\Lambda_{uu} \approx D$, at a constant turbulence intensity level of Tu=3.1%. The variation of the turbulence intensity level, changing from Tu=3.1% to 5.1% was also investigated, with constant turbulence length scale ($\Lambda_{uu} \approx D$), downstream of the biplane grids 2 and 3, respectively. The turbulence intensity level is calculated from the measured mean square velocity $\overline{u'^2}$ and the turbulence length scale is estimated from two different methods, namely (a) Von Karman spectrum data fitting and (b) integration of the velocity autocorrelation curve. The results from these two methods will then be compared relative to each other. The Von Karman spectrum for the streamwise isotropic turbulence can be plotted from,[38]

$$\frac{\phi_{uu}^{VK}(f)U_\infty}{\overline{u'^2}\Lambda_{uu}} = 4\left(1 + \left(\frac{8\pi f \Lambda_{uu}}{3U_\infty}\right)^2\right)^{-5/6}, \tag{1}$$

where $\phi_{uu}^{VK}(f)$ is the Von Karman spectrum.

The comparison between the power spectral density of the velocity fluctuations at $x/D = x$ and the Von Karman spectrum for all the biplane grids is shown in Fig. 3. The results have shown that the power spectral density results of the velocity fluctuations is found to be consistent with the theoretical Von Karman spectrum for all the biplane grids, *i.e.* Grids 1, 2 and 3 with turbulence length scales of Λ_{uu}=0.0152 m 0.0213 m and 0.0239 m, respectively. The isotropic nature of the turbulence flow should have a slope of -5/3, indicating that the flow generated by the biplane grids in this study is isotropic.

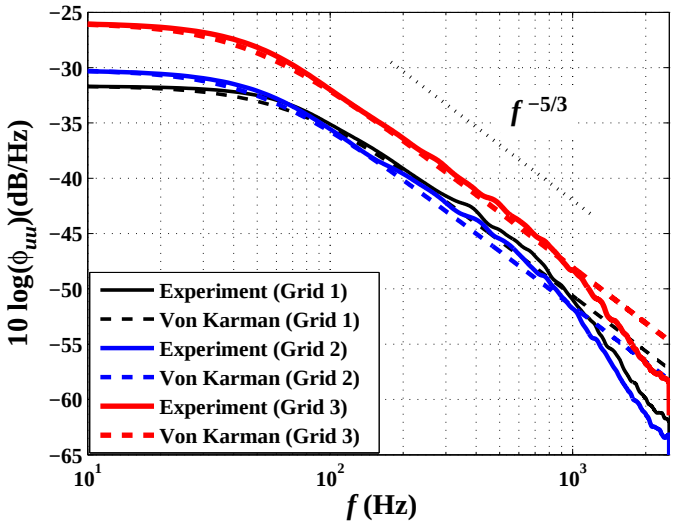

Figure 3: Comparison of the measured streamwise velocity spectrum against Von Karman relation at $Re = 14.7 \times 10^3$.

III. Results and Discussions

A. Aerodynamic characteristics

Figure 4(a) compares the variation of the mean pressure coefficient data measured for all the three biplane grids (turbulent incident flow) against the data measured without the grid (smooth incident flow). Some other experimental data available in the literature at different turbulence intensity levels[14, 39] are also provided for comparison and validation purposes. The mean pressure coefficient results are presented only for the top side of the cylinder model [$\theta = 0^o - 180^o$]. The pressure coefficient minimum point, starting-point of the base region and the base point are denoted by θ_m, θ_s and θ_b for the smooth incident flow and θ_m^G, θ_s^G and θ_b^G for the turbulent incident flows, respectively.

In the favourable pressure gradient region (*i.e.* from the stagnation point to the point of minimum pressure (θ_m and θ_m^G), the pressure coefficient C_p results for the case of the turbulent incident flow are very small at smaller angle, closer to the stagnation point. At higher peripheral angle, the C_p of the turbulent incident flow gradually becomes smaller (more negative) compared to that of the smooth incident flow and reached a maximum difference of C_p at the point of the minimum pressure between the two flows. It can be observed that the pressure coefficient in the turbulent incident flow (with grids) is greater than that in the smooth incident flow (without grid). The pressure coefficient minimum for the smooth incident flow occurs at the angular position $\theta_m = 70^o$. In contrast, the pressure coefficient minimum for the turbulent incident flow shifts to a maximum angular position $\theta_m^G = 75^o$ for all the grids. In the favourable pressure gradient, the reduction in the pressure coefficient is largest for the turbulent flow produced by Grid 1, *i.e.* with smaller turbulence intensity and integral length scale.

The difference between the pressure distributions in the turbulent and smooth incident flows is prominent within the adverse pressure gradient region which stretches from the point of minimum pressure up to the starting point of the base region (θ_s and θ_s^G). In the case of the turbulent incident flow, the C_p becomes much smaller (more negative), with a longer angular extent θ_{sm}^G in the adverse pressure gradient region compared to that of the smooth incident flow condition. The angular range is shown by θ_{sm}^G=[$\theta_s^G - \theta_m^G$] and θ_{sm}=[$\theta_s - \theta_m$] in turbulent and smooth incident flows, respectively. Figure 4 shows that the angular extent is about 10^o in the smooth incident flow and reaches about 15^o in the turbulent incident flow, similar to that of the results observed in.[40] The results have shown that a broader adverse pressure gradient region is observed with the application of Grid 1. This widening of the adverse pressure gradient region leads to a shorter base region which extends from the base region starting point to the base point (θ_b and θ_b^G). The differences between the base regions in both the smooth and turbulent incident flows include a shorter extent and, in

most cases, a higher negative pressure coefficient results is observed in the case of the turbulent incident flow, see Fig. 4. The decrease in the base pressure is due to the increasing curvature of the free streamline and entrainment of the reversed flow into the opposing shear layer, which corresponds to the reduction of the vortex formation length and enhancement of the diffusion length.[14] The angular range is shown by the arc between the base point and the starting point of the base region (or separation angle), *i.e.* θ_{bs}^{G}=$[\theta_{b}^{G} - \theta_{s}^{G}]$ and θ_{bs}=$[\theta_{b} - \theta_{s}]$ in the turbulent and smooth incident flows, respectively. It is obvious that the base region extends over a constant arc at about 100^{o} and 90^{o} in the smooth and turbulent incident flows, respectively. The shortening of the base region leads to a shift in the separation angle. In the base region, the deviation of the pressure coefficient in smooth incident flow with respect to the base pressure coefficient C_{p_b} (C_p at $\theta_b = 180^{o}$) is approximately 3%, which is similar to the base pressure distributions reported in.[41,42] In the case of the turbulent incident flow, the deviation of the pressure coefficient increases to 5.5%, see Fig. 4.

Figure 4(b) shows the comparison of the root-mean-square (rms) pressure coefficient data measured for all the three grids against the data measured without the grid. The rms pressure coefficient($C_{p_{rms}}$) results are presented only for the top side of the cylinder model [$\theta = 0^{o} - 180^{o}$]. In general, the $C_{p_{rms}}$ results show that the turbulent incident flow produces the highest $C_{p_{rms}}$ compared to the smooth incident flow at all the angles. The $C_{p_{rms}}$ for the case of the smooth and turbulent incident flow gradually increases and reached a maximum value at the point of minimum pressure, occurs at the angular position of $\theta_m = 70^{o}$. The $C_{p_{rms}}$, however, gradually becomes smaller at the higher peripheral angle and reached a minimum value (dip) at the angular position of $\theta_m = 120^{o}$. In the base region, it can be observed that both the flows exhibit an overall increase in $C_{p_{rms}}$ between 140^{o}-180^{o}, however, the turbulent incident flows seem to have more effect towards the base. The $C_{p_{rms}}$ results have shown the emergence of a local peak at $\theta_m = 160^{o}$ in the case of the smooth incident flow, and that is shifted to $\theta_m = 170^{o}$ with higher amplitudes in the case of the turbulent incident flows. Moreover, near the base region, the difference between the smooth and turbulent incident flows become more significant towards the base, with a very prominent peak just before the base. The $C_{p_{rms}}$ results for the turbulent incident flows have shown that a much more pronounced behaviour is observed at $\theta_m = 70^{o}$ and $\theta_m = 120^{o}$ with the application of Grid 1. The $C_{p_{rms}}$ results, however, show an insignificant difference between the turbulent incident flow cases, particularly at $\theta_m = 170^{o}$.

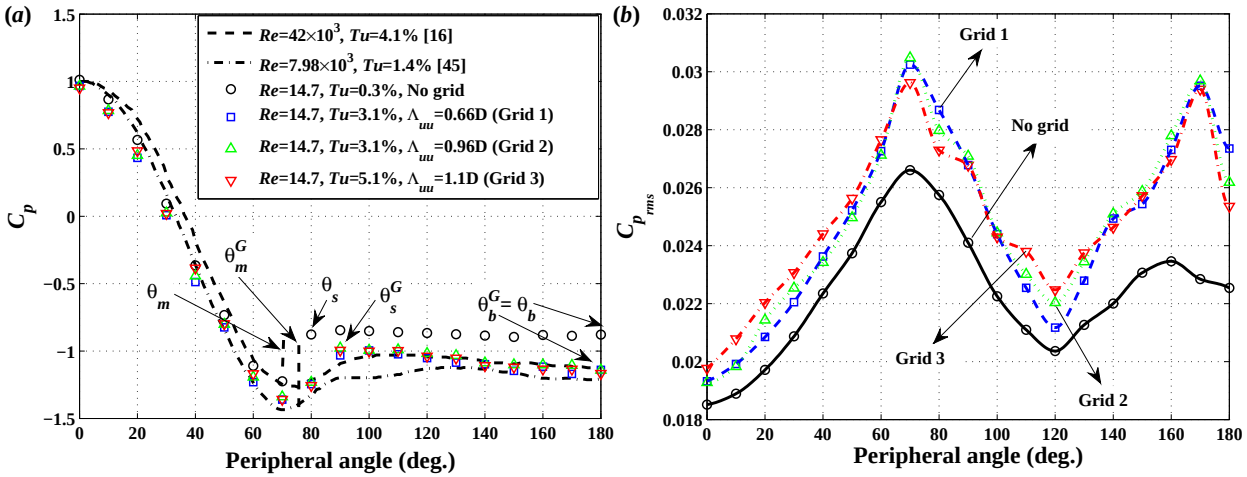

Figure 4: Mean pressure coefficient distributions in turbulent and smooth incident flows at $Re = 14.7 \times 10^3$.

B. Pressure power spectral density

The surface pressure power spectral density (PSD) was measured using microphone *p1* at several peripheral angles, at $Re = 14.7 \times 10^3$ for the smooth and turbulent incident flow (Grids 1, 2 and 3). The surface pressure PSD results are presented in Fig. 5 as a function of the Strouhal number.

The results generally show that the surface pressure PSD spectra consists of both the tonal and broadband components in smooth (without grid) and turbulent (with grids) incident flow. In addition to the fundamental

vortex shedding frequency (f_0), the first two harmonics ($f_1 = 2f_0$ and $f_2 = 3f_0$) are also visible in the PSD results, thanks to the good signal to the background noise ratio. It can be observed from Fig. 5 that there is a significant difference in terms of the frequency location of the dominant tones and broadband trend of the surface pressure PSD results. In the case of the turbulent incident flow, the results have shown that the fundamental tonal frequency has slightly shifted to lower frequencies compared to the smooth incident flow, *i.e.* changes from $St = 0.2$ in the smooth incident flow to about $St = 0.19$ in the turbulent incident flow. This trend is also seen at the first and second harmonics, which is consistent with the results of Hutcheson and Brooks.[24] It can also be observed that the broadband energy content in the turbulent incident flow is generally higher than that of the smooth incident flow in the whole frequency range of interest, which is also prominent at high frequencies and at the post-separation regions ($\theta > \theta_s$).

Results have shown that, in the turbulent incident flow, the tonal frequencies and the broadband part of the surface pressure spectra increases with the turbulent intensity level (Tu=3.1%-5.1%) of the grids (Grids 1,2 and 3). The increase in the tonal and broadband components, in this case, is larger at certain points around the cylinder, *i.e.* at the stagnation point ($\theta = 0^o$), in the developed turbulent boundary layer region ($\theta = 45^o$), near to the separation point ($\theta = 90^o$), in the turbulent region with high intensity level ($\theta = 135^o$) and in the base region where two- and three-dimensional structures are formed ($\theta = 180^o$).

An interesting observation in Fig. 5 is that at ($\theta = 0^o$), the surface pressure PSD in both the smooth and turbulent incident flow is completely broadband and there is no trace of any tonal component. Results have shown that the tonal and broadband contents of the pressure PSD spectra increase with the angle in the pre-separation regions ($\theta \leq \theta_s$).

At $\theta = 15^o$, in the case of the smooth incident flow, the tonal component of the PSD spectra protrudes about 15 dB above the broadband content of the surface pressure, while the tonal features protrude about 5 dB above the broadband content of the surface pressure in the turbulent incident flow cases. For the post-separation locations ($\theta > \theta_s$), the broadband energy content of the pressure spectra generally increases with the angle, while the tonal component of the PSD spectra protrudes even further above the broadband content of the surface pressure. The relative amplitude of the surface pressure for both the smooth and turbulent incident flow are almost similar, *i.e.* the height of the tone becomes similar. It can be observed that at $\theta = 180^o$, the fundamental frequency disappears, and the first harmonic (f_1) remains as the only prominent tonal peak. The amplitude of the tonal frequency at the second harmonics is significant only at the angles close to the separation point ($\theta_s = 80^o, \theta'_s = 90^o$).

Results in Fig 5 have also shown that the slope of the surface pressure PSD changes significantly with frequency and angle, *i.e.* slope here represents the depreciation rate of the turbulence structures. However, it is not easy to find a slope for the broadband content of the surface pressure energy field at small angles and low frequencies because the PSD spectra are dominated by the tonal peaks. One can see from the results at larger angles, particularly beyond the separation point, the broadband content of the surface pressure PSD begins to increase and follows certain f^{-n} decay gradients. For low angle of attack ($\theta = 0^o - 45^o$, the surface pressure PSD spectra follow a gradient of about f^{-1} and $f^{-0.5}$ within $0.1 < St < 0.4$ for the smooth and turbulent incident flows, respectively. The two flows (smooth and turbulent), however, exhibit a similar gradient profile of about $f^{-3.5}$ and f^{-5} in the mid- and high-frequency regions, after first harmonic, respectively. The gradients found are, however, different at small angles. At large angles ($\theta > 135^o$), and particularly at the cylinder base ($\theta > 180^o$), the broadband slope changes greatly with frequency and follow a gradient of about $f^{-1.5}$ within $0.8 < fD/U_o < 2$ and f^{-2} at high frequencies ($fD/U_o > 3$). The behaviour of the spectra becomes very similar apart from a change in the magnitude of the pressure fluctuations.

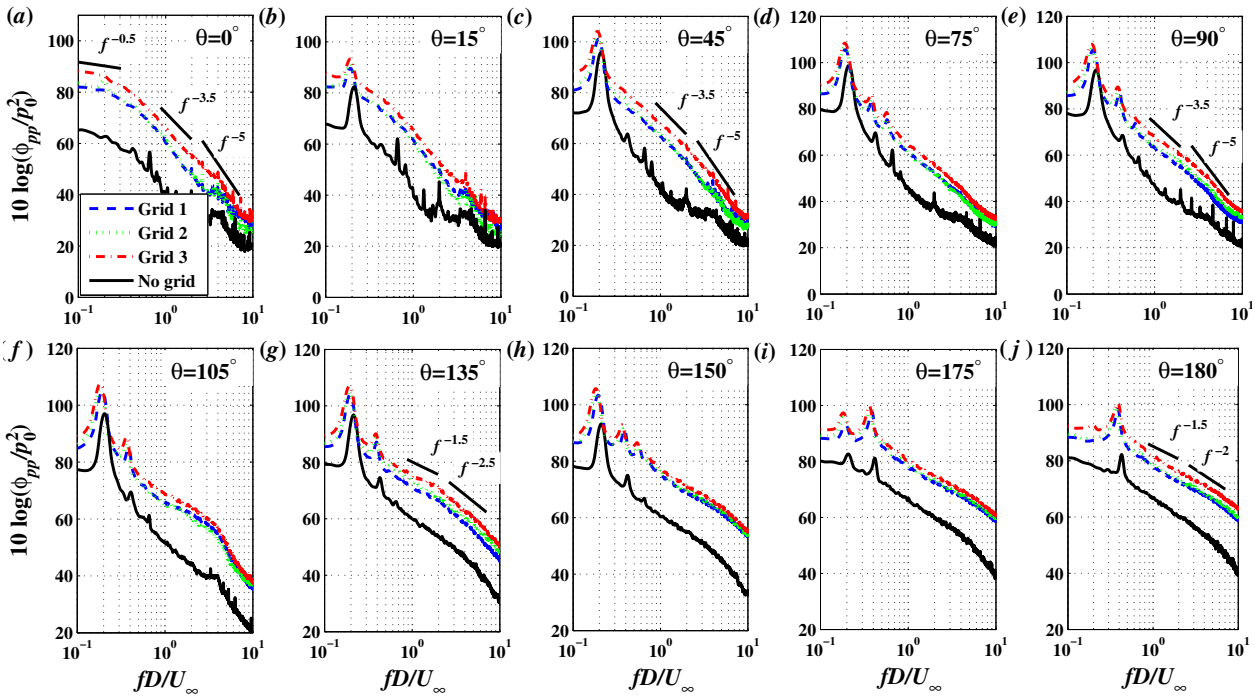

Figure 5: Surface pressure power spectral density measured at different angular positions at $Re = 14.7 \times 10^3$.

1. *Lateral coherence*

The lateral coherence results measured between the spanwise transducers $p1$ and $p2$, with several separation distances at selected angular positions (θ=0^o, 45^o, 90^o, 135^o and 180^o) are presented in Fig. 6. The coherence function between two pressure transducers along the span and streamwise directions can be found from,

$$\gamma^2_{pi,pj}(\eta_z, f) = \frac{|\Phi_{pi,pj}(\eta_z, f)|^2}{\Phi_{pi,pi}(\eta_z, f)\Phi_{pj,pj}(\eta_z, f)}, \tag{2}$$

where $\Phi_{pi,pj}(\eta_z, f)$ denotes the cross-spectrum between the two pressure signals, $\Phi_{pi,pi}(\eta_z, f)$ is the auto-spectrum of each individual signal, and η_z is the spanwise separation distance between the transducers.

The figure is plotted as a function of Strouhal number at a free-stream velocity of $U_\infty = 10\ m/s$ (Re=14.7 $\times$ 10^3) for smooth and three types of turbulent incident flows. In order to sufficiently capture the two- and three-dimensional flow structures around the cylinder, the coherence measurements have been performed for the lateral spacings within the range of $0.41 \leq \eta_z/D \leq 5.95$. The results in Fig. 6 generally show that the lateral coherence level between the transducers decreases with η_z/D at all angles. Results have shown that at all angles around the cylinder, the maximum coherence occurs at the fundamental vortex shedding frequency (f_0) and its harmonics (f_1 and f_2). It also can be seen that the coherence value at f_0 is greater than those at f_1 and f_2 for all angles, except for $\theta = 180^o$, which is mainly dominated by the tonal component at f_1. The coherence values at f_0 and f_2 , however, reduces to nearly zero. The results also indicate that despite the emergence of the strong peaks at f_0, f_1 and f_2, the coherence results for the transducers in small lateral spacings $\eta_z/D = 0.41 - 0.68$ experience a relatively strong broadband content. However, the coherence becomes tonal and reaches zero at other frequencies with increasing η_z/D, *i.e.* $\eta_z/D > 0.68$. This signifies that the vortex shedding structures (*i.e.* two-dimensional structures) withhold their coherence over a larger spanwise distance relative to that of the three-dimensional flow structures. For the lateral spacing distance of $\eta_z/D = 0.41 - 2.27$, at $\theta = 0^o$, the coherence results show a broadband behaviour with a distinct tonal peak at f_0, indicating that the lift fluctuation can be discerned at the stagnation point. Moving downstream, the tonal and broadband contents of the lateral coherence are observed to be strongest at $\theta = 45^o$, which

is believed to be due to the development of larger turbulent flow structures. The broadband coherence, however, gradually decreases at the post-separation region ($\theta = 90^o$) and turbulent flow region ($\theta = 135^o$) and reaches zero at $\theta = 180^o$. At a larger lateral spacing distance ($\eta_z/D = 5.95$), it can be seen that the tonal and broadband coherence for all the cases (*i.e.* smooth and turbulent incident flows) reduces to entirely zero at $\theta = 0^o$ and $\theta = 180^o$. At $\theta = 45^o$ to $\theta = 135^o$, a much smaller coherence value is observed at the fundamental shedding frequency, indicating that vortex shedding structures retain their coherence in the post-separation and turbulent flow regions. The coherence of the two-dimensional structures at f_1 within $0.41 \leq \eta_z/D \leq 0.68$ for smooth incident flow is smaller than that of the turbulent incident flow at all angles. These behaviour, however, can only be seen at $\theta = 90^o$ for $\eta_z/D \leq 0.68$. Results have also shown that with increasing lateral spacing from $\eta_z/D = 0.68$ to $\eta_z/D = 2.27$, the coherence difference between the smooth and turbulent flows at f_1 increases rapidly for angles around the separation point (*i.e.*, $\theta = 45^o$, $\theta = 90^o$ and $\theta = 135^o$).In the case of the turbulent incident flow, the strongest tonal and broadband coherence at the fundamental vortex shedding frequency occurs via the application of Grid 3 for smaller transducers spacings ($0.41 \leq \eta_z/D \leq 0.68$), while at larger transducers separation distances ($\eta_z/D > 0.68$), the strongest tonal behaviour at f_1 occurs via the application of Grid 2.

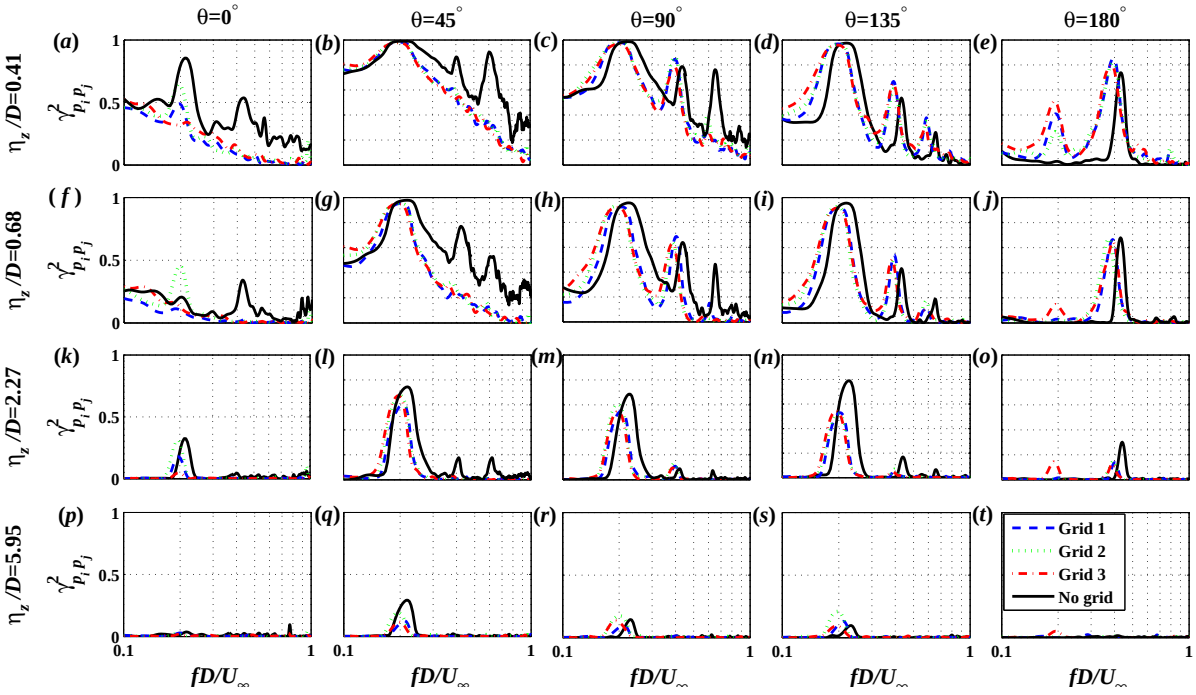

Figure 6: Lateral coherence measured between several spanwise locations at different angular positions at $Re = 14.7 \times 10^3$.

2. *Surface pressure spanwise length-scale*

Figure 7 shows the frequency dependent spanwise length-scale results at different angles. The spanwise length-scale of the surface pressure fluctuations along the span of the cylinder is calculated as,

$$\lambda_{pp}(f) = \int_0^\infty \sqrt{\gamma^2_{pi,pj}(f, \eta_z) d\Delta z}. \tag{3}$$

In both the smooth and turbulent incident flow cases, the results for $\theta = 90^o$ and 135^o show a distinct tonal peaks at the fundamental shedding frequency (f_0) and its harmonics (f_1 and f_2). For $\theta = 0^o$, only the fundamental shedding tone is observed, while for $\theta = 180^o$, the tonal peaks occur at f_1 for all the cases except for turbulence generated by the Grid 3, where the tonal peak occurs at the fundamental shedding frequency. In the case of the smooth incident flow, the correlation length-scale value for $\theta = 0^o$ at f_0 reaches about $\lambda_{pp}(f_0) \approx 5D$, while that for $\theta = 45^o$, the value increases up to $\lambda_{pp}(f_0) \approx 8.4D$. The spanwise length-scale

values at $\theta = 90^o$ and $\theta = 135^o$, then becomes slightly less than that of the $\theta = 45^o$ at other frequencies, signifying the existence of a more three-dimensional flow structures. The correlation length-scale value for the f_1 and f_2 at $\theta = 45^o, 90^o$ and 135^o are $\lambda_{pp}(f_1) \approx 4.2D$ and $\lambda_{pp}(f_2) \approx 4D$, respectively. In the case of the turbulent incident flow, the general trend of the results at f_0, f_1 and f_2 are similar to that of the smooth incident flow, but with a much smaller correlation length at all angles, except for $\theta = 180^o$, which is consistent with the results observed in Fig. 6. The results in Fig. 7 indicate that the spanwise correlation length is the largest for the turbulent incident flow generated by the Grid 3, *i.e.* with higher turbulence intensity level and velocity correlation length, while the spanwise correlation length is found to be the smallest for the turbulent incident flow case with lower turbulence intensity level and moderate velocity correlation length (Grid 2) compared to that of Grid 1, at all angles. These general trend of the results, however, is not observed at the cylinder base region ($\theta = 180^o$), where the length-scales of the turbulent incident flows is the highest at the low-frequency, *i.e.* f_0, compared to that of the smooth incident flow, however, the peak at f_1 is mainly dominated by the flow structures without the application of the biplane grids. The correlation length-scales results for all the turbulent flow incident cases, however, becomes constant at high frequencies.

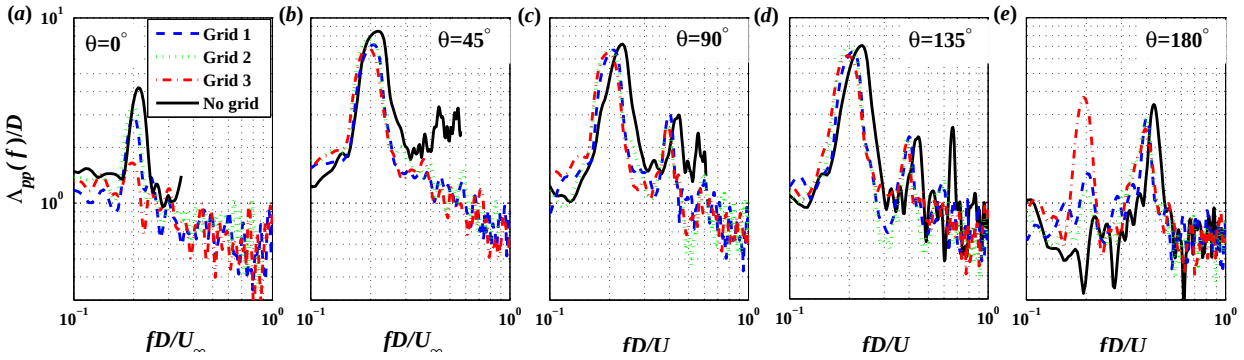

Figure 7: Frequency-dependent spanwise length-scales of the surface pressure fluctuations at different angular position at $Re = 14.7 \times 10^3$.

IV. Conclusion

The present study is concerned with the experimental investigation on the effects of the turbulent incoming flow on the surface pressure fluctuations acting on a cylinder in a cross-flow. The work has been carried out using a highly instrumented test rig, equipped with several peripheral and spanwise surface pressure transducers. The results have shown that the surface pressure power spectral density at the fundamental vortex shedding and its harmonics can be reduced significantly in the case of the turbulent incident flow compared to that of the smooth incident flow. In the case of the turbulent incident flow, the results have shown that the fundamental tonal frequency has slightly shifted to lower frequencies compared to the smooth incident flow. The two-dimensionality of the vortex shedding structures along the cylinder span has been studied using the lateral coherence of the surface pressure fluctuations. Results have shown that, in the case of the smooth and turbulent incident flow, the surface pressure fluctuations remains highly coherent over a long distance along the cylinder span length at the fundamental shedding frequency f_0, while for f_1 and f_2, the coherence decays much quicker over a much shorter cylinder span length. The general trend of the correlation length results at f_0, f_1 and f_2 are similar in both of the smooth and turbulent incident flow case, but with a much smaller correlation length at most of the angles in the case of the turbulent incident flow. The results in this paper have shown the fundamental aerodynamic and aeroacoustic studies on turbulent flow interaction with a circular cylinder, and provide the motivation for more high-quality computational studies in the context of noise generation mechanisms of bluff bodies.

References

[1]Maryami, R., Azarpeyvand, M., Dehghan, A., and Afshari, A., "An Experimental Investigation of the Surface Pressure Fluctuations for Round Cylinders," *Journal of Fluids Engineering*, Vol. 141, No. 6, 2019, pp. 061203.

[2]Showkat Ali, S. A., Azarpeyvand, M., and da Silva, C. R. I., "Trailing-edge flow and noise control using porous treatments," *Journal of Fluid Mechanics*, Vol. 850, 2018, pp. 83–119.

[3]Schlinker, R. and AMIET, R., "Vortex noise from nonrotating cylinders and airfoils," *14th Aerospace Sciences Meeting*, 1976, p. 81.

[4]Showkat Ali, S. A., Azarpeyvand, M., Szőke, M., and Ilário da Silva, C. R., "Boundary layer flow interaction with a permeable wall," *Physics of Fluids*, Vol. 30, No. 8, 2018, pp. 085111.

[5]West, G. and Apelt, C., "Measurements of fluctuating pressures and forces on a circular cylinder in the reynolds number range 104 to 2· 5× 105," *Journal of Fluids and Structures*, Vol. 7, No. 3, 1993, pp. 227–244.

[6]Showkat Ali, S. A., Szoke, M., Azarpeyvand, M., and Ilario da Silva, C. R., "Turbulent Flow Interaction with Porous Surfaces," *24th AIAA/CEAS Aeroacoustics Conference, AIAA 2018-2801*.

[7]Stowell, E. Z. and Deming, A. F., "Vortex noise from rotating cylindrical rods," *The Journal of the Acoustical Society of America*, Vol. 7, No. 3, 1936, pp. 190–198.

[8]Showkat Ali, S. A., Azarpeyvand, M., and Ilario da Silva, C. R., "Trailing Edge Bluntness Flow and Noise Control Using Porous Treatments," *22nd AIAA/CEAS Aeroacoustics Conference, AIAA 2016-2832*.

[9]Showkat Ali, S. A., Azarpeyvand, M., and Ilario da Silva, C. R., "Experimental Study of Porous Treatment for Aerodynamic and Aeroacoustic Purposes," *23rd AIAA/CEAS Aeroacoustics Conference, AIAA 2017-3358*.

[10]Oguma, Y., Yamagata, T., and Fujisawa, N., "Measurement of sound source distribution around a circular cylinder in a uniform flow by combined particle image velocimetry and microphone technique," *Journal of Wind Engineering and Industrial Aerodynamics*, Vol. 118, 2013, pp. 1–11.

[11]Showkat Ali, S. A., Liu, X., and Azarpeyvand, M., "Bluff Body Flow and Noise Control Using Porous Media," *22nd AIAA/CEAS Aeroacoustics Conference, AIAA 2016-2754*.

[12]Bilka, M. J., Kerrian, P., Ross, M. H., and Morris, S. C., "Radiated sound from a circular cylinder in a turbulent shear layer," *International Journal of Aeroacoustics*, Vol. 13, No. 7-8, 2014, pp. 511–532.

[13]Bloor, M. S., "The transition to turbulence in the wake of a circular cylinder," *Journal of Fluid Mechanics*, Vol. 19, No. 2, 1964, pp. 290–304.

[14]Norberg, C., "Interaction between freestream turbulence and vortex shedding for a single tube in cross-flow," *Journal of wind engineering and industrial aerodynamics*, Vol. 23, 1986, pp. 501–514.

[15]Norberg, C. and Sunden, B., "Turbulence and Reynolds number effects on the flow and fluid forces on a single cylinder in cross flow," *Journal of Fluids and Structures*, Vol. 1, No. 3, 1987, pp. 337–357.

[16]Casalino, D. and Jacob, M., "Prediction of aerodynamic sound from circular rods via spanwise statistical modelling," *Journal of Sound and Vibration*, Vol. 262, No. 4, 2003, pp. 815–844.

[17]Fujita, H., Suzuki, H., Sagawa, A., and Takaishi, T., "The Aeolian tone and the surface pressure in high Reynolds number flow," *6th Aeroacoustics Conference and Exhibit*, 2000, p. 2002.

[18]Ackerman, J., Gostelow, J. P., Rona, A., and Carscallen, W. E., "Measurements of Fluctuating Pressures on a Circular Cylinder in Subsonic Cross Flow," *AIAA journal*, Vol. 47, No. 9, 2009, pp. 2121–2131.

[19]Curle, N., "The influence of solid boundaries upon aerodynamic sound," *Proceedings of the Royal Society of London. Series A. Mathematical and Physical Sciences*, Vol. 231, No. 1187, 1955, pp. 505–514.

[20]Garcia-Sagrado, A. and Hynes, T., "Wall pressure sources near an airfoil trailing edge under turbulent boundary layers," *Journal of Fluids and Structures*, Vol. 30, 2012, pp. 3–34.

[21]Barlow, J. B., Rae Jr, W. H., and Pope, A., "Low speed wind tunnel testing," *INCAS Bulletin*, Vol. 7, No. 1, 2015, pp. 133.

[22]Wilkins, S. J. and Hall, J. W., "Experimental investigation of a tandem cylinder system with a yawed upstream cylinder," *Journal of Pressure Vessel Technology*, Vol. 136, No. 1, 2014, pp. 011302.

[23]Goody, M. C. and Simpson, R. L., "An experimental investigation of pressure fluctuations in three-dimensional turbulent boundary layers," Tech. rep., Virginia Tech., 1999.

[24]Hutcheson, F. V. and Brooks, T. F., "Noise radiation from single and multiple rod configurations," *International Journal of Aeroacoustics*, Vol. 11, No. 3-4, 2012, pp. 291–333.

[25]Afshari, A., Azarpeyvand, M., Dehghan, A. A., and Szoke, M., "Effects of Streamwise Surface Treatments on Trailing Edge Noise Reduction," *23rd AIAA/CEAS Aeroacoustics Conference*, 2017, p. 3499.

[26]Bendat, J. S. and Piersol, A. G., *Random data: analysis and measurement procedures*, Vol. 729, John Wiley & Sons, 2011.

[27]Yavuzkurt, S., "A guide to uncertainty analysis of hot-wire data," *ASME, Transactions, Journal of Fluids Engineering*, Vol. 106, No. 2, 1984, pp. 181–186.

[28]Corrsin, S., "Turbulence: experimental methods," *Handbuch der Physik*, Vol. 3, 1963, pp. 524–590.

[29]Uberoi, M. S. and Wallis, S., "Effect of grid geometry on turbulence decay," *The Physics of Fluids*, Vol. 10, No. 6, 1967, pp. 1216–1224.

[30]Laws, E. and Livesey, J., "Flow through screens," *Annual review of fluid mechanics*, Vol. 10, No. 1, 1978, pp. 247–266.

[31]Mohamed, M. S. and LaRue, J. C., "The decay power law in grid-generated turbulence," *Journal of Fluid Mechanics*, Vol. 219, 1990, pp. 195–214.

[32]Comte-Bellot, G. and Corrsin, S., "The use of a contraction to improve the isotropy of grid-generated turbulence," *Journal of fluid mechanics*, Vol. 25, No. 4, 1966, pp. 657–682.

[33]Ling, S. and Huang, T., "Decay of weak turbulence," *The Physics of Fluids*, Vol. 13, No. 12, 1970, pp. 2912–2924.

[34]Hearst, R. J. and Lavoie, P., "Decay of turbulence generated by a square-fractal-element grid," *Journal of Fluid Mechanics*, Vol. 741, 2014, pp. 567–584.

[35]Krogstad, P.-Å. and Davidson, P., "Freely decaying, homogeneous turbulence generated by multi-scale grids," *Journal of Fluid Mechanics*, Vol. 680, 2011, pp. 417–434.

[36]Lavoie, P., Djenidi, L., and Antonia, R., "Effects of initial conditions in decaying turbulence generated by passive grids," *Journal of Fluid Mechanics*, Vol. 585, 2007, pp. 395–420.

[37]Lavoie, P., Burattini, P., Djenidi, L., and Antonia, R. A., "Effect of initial conditions on decaying grid turbulence at low R λ," *Experiments in fluids*, Vol. 39, No. 5, 2005, pp. 865–874.

[38]Hinze, J., "Turbulence McGraw-Hill," *New York*, Vol. 218, 1975, pp. 457.

[39]Norberg, C., "Effects of Reynolds number and a low-intensity freestream turbulence on the flow around a circular cylinder," *Chalmers University, Goteborg, Sweden, Technological Publications*, Vol. 87, No. 2, 1987, pp. 1–55.

[40]Sadeh, W. Z. and Saharon, D. B., "Turbulence effect on crossflow around a circular cylinder at subcritical Reynolds numbers," 1982.

[41]Fage, A., "Further experiments on the flow around a circular cylinder," *Aero. Res. Coun.*, Vol. 1369, 1931.

[42]Weidman, P. D., *Wake transition and blockage effects on cylinder base pressures*, Ph.D. thesis, California Institute of Technology, 1968.